Brain Stimulation 19 (2026) 103013

Contents lists available at ScienceDirect

Brain Stimulation

journal homepage: www.journals.elsevier.com/brain-stimulation

A wireless, 60-channel, AI-enabled neurostimulation platform

Daniel S. Rizzuto [a], Haydn G. Herrema [a], Zhe Hu [a], Daniil Utin [a], Joshua Kahn [a], Chris Ho [a], Andrew B. Smiles [a], Robert E. Gross [b], Bradley C. Lega [c], Sandhitsu R. Das [d], Michael J. Kahana [a,*]

[a] Nia Therapeutics, Inc., Allston, 02134, MA, USA
[b] Department of Neurosurgery, Rutgers University, New Brunswick, 08901, NJ, USA
[c] Department of Neurology and Neurotherapeutics, University of Texas Southwestern, Dallas, 75390, TX, USA
[d] Department of Neurology, University of Pennsylvania, 19104, PA, USA

ARTICLE INFO

Keywords:
Brain computer interface
Neuromodulation
Artificial intelligence
Human memory
Biomarkers

ABSTRACT

Objective: Closed-loop neuromodulatory therapies require devices that can decode ongoing brain states and deliver multi-site stimulation.
Methods: We describe the Smart Neurostimulation System (SNS), a cranially mounted implant with 60 configurable recording/stimulation channels, inductive power, and onboard spectral-feature classification. In three freely-moving sheep, we streamed local-field potentials and conducted two parameter-sweep experiments.
Results: Cross-validated movement classifiers achieved an average AUC exceeding 0.95. Increasing stimulation amplitude and frequency produced post-stimulation elevations in α-band (8–12 Hz) and γ-band (78–82 Hz) power at most target locations.
Conclusion: The SNS unifies high-density sensing, real-time brain state decoding, and programmable closed-loop stimulation in a single device, demonstrating behavioral-state prediction and parameter-dependent neuromodulation in vivo.
Significance: These findings establish a preclinical foundation for biomarker-guided stimulation targeting distributed cortical networks underlying memory and cognition.

Introduction

Closed-loop neuromodulation — which adapts in real time to the brain's evolving state — offers a path to more effective and safer therapies across a wide range of neurological conditions. In epilepsy, responsive neurostimulation cuts seizure burden by stimulating the brain only when it senses pre-ictal EEG patterns [1]. In Parkinson's disease and essential tremor, adaptive deep-brain stimulation raises efficacy while reducing dyskinesias [2]. In chronic pain and depression, state-contingent stimulation promises symptom relief without the habituation and mood swings seen with fixed schedules [3–7]. These gains arise because closed-loop devices tailor pulse timing, location, and amplitude to moment-by-moment neural activity rather than relying on clinician-programmed settings that may be optimal only under the static conditions present at the time of programming.

Despite these clinical gains, today's adaptive systems still rely on a strikingly small information footprint. Medtronic's *Percept*™ aDBS, for example, modulates amplitude from a single β-band power estimate per subthalamic lead, whereas the NeuroPace *RNS*® system for epilepsy responds to band-pass or line-length thresholds on up to four bipolar recording channels. Such low-dimensional control cannot capture the distributed, multifrequency dynamics that underlie higher-order functions such as memory, attention, or mood. Treating these complex indications, therefore, requires sampling many sites spanning distributed brain networks, extracting numerous spectral and temporal features simultaneously, and combining those features with a real-time classifier capable of predicting momentary fluctuations in neurocognitive state. Prior work has shown that multivariate classifiers trained on hundreds of spectral features can reliably decode moments of high vs. low mnemonic efficacy in humans [8–11]. Delivering such classifier-based closed-loop therapy, however, demands implants that record from many distributed sites, process spectral features onboard, and perform sensing and stimulation concurrently, all while remaining small, wireless, and power-efficient for chronic use.

Here we describe progress toward developing and testing a wireless, 60-channel, AI-enabled brain–computer interface, the Smart Neurostimulation System (SNS). Our proof-of-concept studies of closed-loop neuromodulation to improve memory motivated the SNS design [12,

* Corresponding author.
E-mail address: mjkahana@niatx.com (M.J. Kahana).

https://doi.org/10.1016/j.brs.2025.103013
Received 7 July 2025; Received in revised form 19 November 2025; Accepted 18 December 2025
Available online 20 December 2025

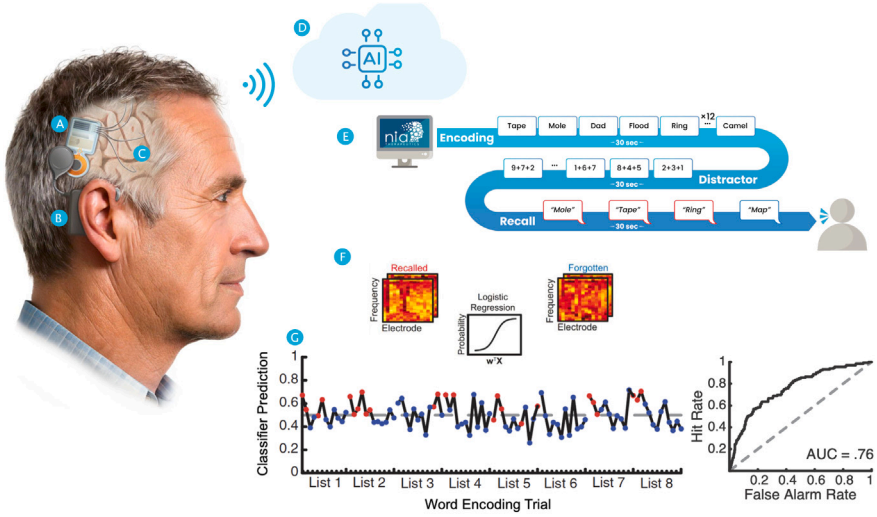

Fig. 1. The Smart Neurostimulation System. Artistic rendering of the SNS in clinical use, including (a) a cranial implant responsible for neural sensing and stimulation; (b) a wearable External Processor providing power and acting as a communications hub; (c) four depth leads with a total of 64 contacts; and (d) a cloud-based AI platform that connects to the SNS via a Clinical Programmer device or Mobile App. Clinicians optimize the therapy for each patient using the programmer. Patients perform delayed recall tasks (e) while the SNS analyzes spectral features (f) learning to predict, in hold-out sessions, which list items subjects will remember (red dots) or forget (blue dots) (g). The SNS uses these models to trigger stimulation during predicted memory lapses and to optimize stimulation parameters.

13]. These studies, conducted in epilepsy patients with and without a prior history of traumatic brain injury (TBI), used external devices connected to a host PC to record brain activity and to apply stimulation through commercially available, FDA-cleared electrodes. Neurosurgeons implanted these electrodes semi-chronically to map seizure activity and brain function to guide potential resective surgery

Predicting momentary variability in human cognitive function motivated the requirements for the SNS. Mnemonic ability varies from trial to trial within the same individual, with the largest predictor being performance on the prior trial [14]. Spectral analyses of intracranial recordings show that these fluctuations arise from large-scale network dynamics spanning lateral temporal, medial temporal, and prefrontal cortices. Reliable prediction of memory success requires simultaneous sampling from dozens of electrodes and the use of multivariate models that integrate information across frequencies and regions [10,11,15]. These findings highlight the need for a neural interface capable of wide-area sensing, real-time spectral estimation, and rapid classifier-based control of stimulation.

Mnemonic effects of electrical stimulation depend on brain state: stimulation impaired memory when delivered during classifier-predicted good states and improved memory when delivered during classifier-predicted poor states [8]. In a subsequent study, we validated these observations by designing a closed-loop system that triggered high-frequency (100–200 Hz) stimulation bursts upon detected memory lapses, reliably improving memory for stimulated items [9]. A replication in a cohort ($N = 8$) of epilepsy patients with moderate-to-severe TBI further showed that the mnemonic benefits of closed-loop stimulation accrue to the entire stimulated list, not just to the stimulated items [12]. Analyses of a larger cohort of patients ($N = 47$) found that only stimulation near white-matter tracts yielded consistent list-level mnemonic benefits; among these targets, those with the strongest functional connectivity to the memory network produced greater mnemonic boosts [13].

These studies provide proof of concept for a brain–computer interface therapy for memory loss. Approved devices, however, cannot meet the multichannel sensing and closed-loop stimulation requirements of such a therapy. To satisfy these requirements, we designed the SNS.

The Smart Neurostimulation System (SNS)

Fig. 1 illustrates the overall system design. The SNS comprises a cranially mounted implantable pulse generator (IPG) for processing neural data and controlling therapy delivery; a wearable external processor (EP) that powers the IPG and acts as a communication hub; four custom depth leads for sensing and stimulating neural tissue; and a physician programmer and cloud-based AI platform developed for personalizing therapy in human studies. During therapy personalization, the SNS records multi-channel field potentials while patients study and recall word lists, Fig. 1E. Standardized delayed-recall tasks serve as validated surrogates for everyday memory, with performance predicting functional outcomes, such as return to work, in TBI cohorts [16,17].

Applying spectral filters to the EEG data enables the IPG to estimate LFP power at frequencies from 3–180 Hz. The spectral filters employ a standard Goertzel algorithm [18] for estimating signal power at a specific frequency. The firmware specifies the filter coefficients, which can be easily updated. Machine-learning models trained on these spectral features predict mnemonic success (Fig. 1F) and drive later closed-loop stimulation decisions during therapy (Fig. 1G).

Fig. 2 shows the manufactured IPG, EP, and Depth Leads. The IPG senses local field activity from 60 electrodes (plus four fixed reference electrodes), processes the data and controls therapy delivery. The EP inductively powers the IPG and relays data over a 2.2 Mbit/s link, sufficient to stream (500-Hz sampled) signals from every channel, with reliable transmission across 5–10 mm of scalp.

The EP serves as the system's communication hub, providing USB for high-speed communication to the Programmer and Bluetooth low energy (BLE) for low-bandwidth mobile-app telemetry. The SNS end-to-end authenticates and encrypts all commands and responses using 128-bit AES-GCM, ensuring only authenticated users and devices can connect to the device, and preventing administration of malicious therapy parameters. As with cochlear implants, users recharge the EP overnight, outside therapy hours. The preclinical version of the EP demonstrated here has 256 Mbits of on-board FLASH storage, capable of storing 30 min of spectrally-transformed neural data from all 60 sensing channels. The clinical release of the EP will include 2Gbits of storage, capable of storing more than 4 h of spectrally-transformed neural data from all 60 sensing channels. During clinician programming over a USB connection, the programmer laptop operates on battery

Fig. 2. The Smart Neurostimulation System prototype, including (a) the implantable pulse generator; (b) the external processor; and (c) depth leads containing up to 16 electrodes each. All device materials were selected for biocompatibility and prior medical device usage. The silicone-encapsulated IPG houses a hermetically sealed titanium can surrounding the embedded electronics, platinum/iridium, stainless steel and Pellethane in the lead connector assembly, and Parylene-C surrounding the gold-coated magnet. The depth lead utilizes platinum/iridium electrodes, a stainless-steel set screw block, and a pellethane lead body. EP materials include ABS plastic, nylon and silicone. A U.S. quarter illustrates the scale of the device.

power, eliminating any connection between the EP and the power mains. During routine at-home use, the EP transfers data to the Cloud each night via a BLE connection to the user's mobile phone.

The SNS design arose from a need to meet three constraints: (i) recording field potentials from ~64 electrodes in widespread brain locations at sampling rates ≥ 500 Hz (to discern high-frequency signals that predict mnemonic function [19,20]); (ii) delivering rapid stimulation bursts triggered by onboard machine-learning models that predict memory lapses; and (iii) fitting within a cranial form factor proven safe in prior applications (e.g., the NeuroPace RNS).

To estimate the minimum number of electrodes required to achieve classification performance comparable to that reported in our prior studies [12,13], we conducted a feature subset resampling analysis using publicly available intracranial EEG data from the Restoring Active Memory project [21]. We identified participants with at least 128 recording channels and trained penalized logistic regression classifiers to predict mnemonic success from spectral features of EEG activity measured during word encoding. For each iteration, we randomly sampled subsets of 4, 8, 16, 32, or 64 electrodes and computed the cross-validated area under the receiver operating characteristic curve (AUC). Relative to classifiers trained on the full feature set, we observed statistically significant reductions in AUC for models trained on subsets of 4, 8, 16, or 32 electrodes. In contrast, performance for models trained on 64 electrodes did not differ significantly from that obtained using all channels (both mean AUC ~ 0.62, evaluated on held-out sessions). These findings indicate that approximately 64 channels are sufficient to reproduce the decoding performance achieved in our closed-loop stimulation studies, thereby supporting the feasibility of memory-state classification with the SNS.

The EP and IPG communicate via an inductive link composed of two conductive coils (see Fig. 3A,B). Command and response data flow bidirectionally through this link, while the IPG simultaneously transmits neural data to the EP. The EP can then send neural data to a PC over USB or to a mobile phone via BLE. A microcontroller (MCU) in the EP controls most of the system logic, including communication, safety systems, and firmware updates. A field programmable gate array (FPGA) controls the inductive link communication protocol on both the EP and the IPG. Power management hardware on the IPG regulates power input, while MCUs on the IPG and EP process all communication messages and manage therapy safety.

Fig. 3C illustrates the electrical interface between IPG and neural tissue. The IPG lead interface holds four leads with 16 electrodes each. Sixty of the 64 platinum-iridium electrodes can sense and stimulate neural tissue; a central electrode on each lead serves as an electrical reference. On the IPG, a proprietary Application-Specific Integrated Circuit (ASIC) connects to the electrode contacts through DC-blocking capacitors. This custom ASIC was designed specifically for brain interfaces to provide sensing and stimulation capabilities [22,23]. Inside the ASIC, there are 64 channels for sensing and stimulation, one for each electrode contact. The ASIC has four independent current sources that can multiplexed to any of the 64 channels, delivering square-wave, charge-balanced, biphasic pulses. At the system level, our software for the forthcoming clinical trial limits stimulation to two simultaneous bipolar targets. For our clinical application, neural data is only analyzed during the post-stimulation periods to avoid contamination with stimulation artifact.

The SNS firmware architecture (Fig. 4) supports command and control, battery management, firmware updates, event logging, and over-the-air updates. The firmware operates in two modes: (i) Therapy Personalization and (ii) Therapy Delivery. Therapy Personalization mode supports the transmission of raw 500-Hz LFP data from the IPG to an external PC (via the EP) for offline processing and storage (see *Streaming Path* Fig. 4). Therapy Delivery mode supports spectral processing, brain state classification and stimulation delivery (see *Therapy Delivery path* in Fig. 4). In this mode, the IPG estimates spectral power and makes therapy decisions every 128 ms. If the classifier indicates that therapy should be applied, the IPG applies electrical stimulation to the brain within 25 ms of the last neural data sample entering the buffer. Therapy parameters, including target electrodes, stimulation amplitude (0.02–5.0 mA), frequency (15–256 Hz), pulse width (16-500 usec), and duration (1-2000 msec) are configurable by the user. Therapy Delivery mode also supports the streaming of processed (spectrally transformed) neural data from the IPG to the EP for offline processing and storage. The IPG utilizes cyclic on-off keying (COOK) for high-speed data transmission [24], passively modulates the inductive field for efficient communication [25], and has been designed to operate continuously while staying within safe thermal limits as set by ISO 14708-1 [26].

Table 1
Animal characteristics and depth leads implanted into left and right hemispheres. All animals had one SNS IPG implanted at the bottom of the neck and one depth lead placed into each hemisphere. In animal S001, one 8-channel SNS depth lead was placed in left hemisphere and a Medtronic Control lead (model 3387S-40) was placed in right hemisphere. All other animals had SNS 8-channel depth leads placed into each hemisphere.

Animal	Sex	Breed	Age (mo.)	Weight (kg)		Lead type	
				Start	End	Left	Right
S001	Female	Polypay	18	60.3	70.5	SNS	Control
S002	Female	Polypay	10	48.5	56.1	SNS	SNS
S003	Female	Polypay	10	50.5	58.0	SNS	SNS

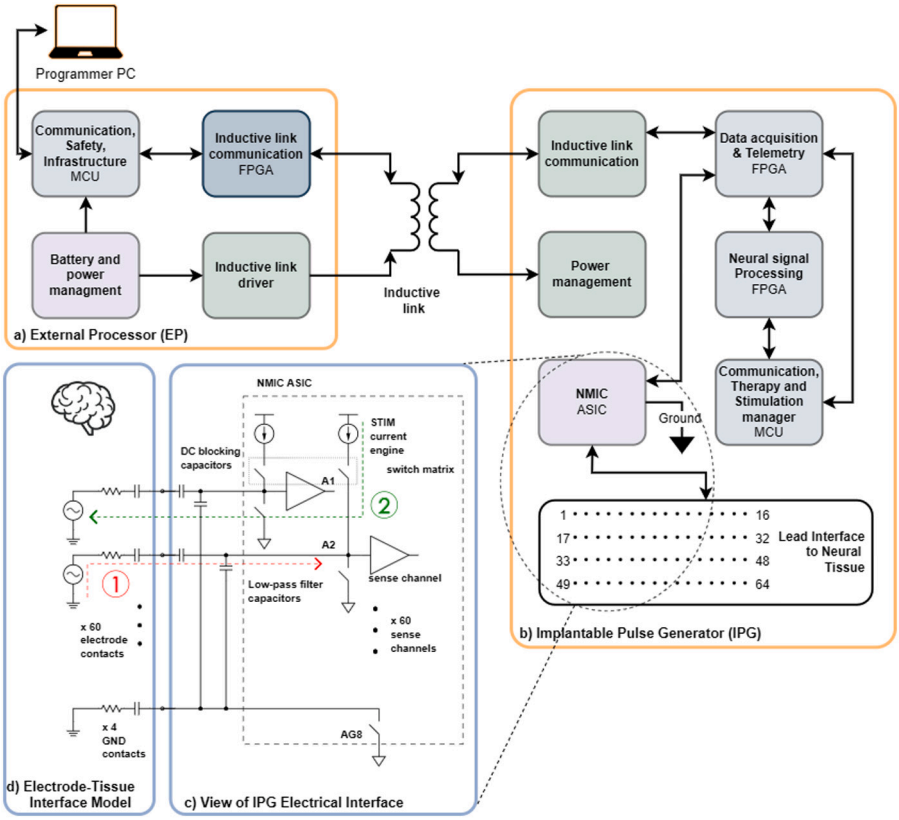

Fig. 3. The SNS system hardware and electrical interface schematic. (a) the External Processor (EP), and (b) the Implantable Pulse Generator (IPG). (c) Expanded view of the electrical interface between the stimulation/sensing ASIC (Neuromodulation Integrated Circuit; NMIC) and the leads. (d) the Electrode-Tissue interface R-C model. Information (data or commands) can be sent via the EP (a) to the IPG (b) and in reverse. The IPG records neural data via (c) and transmits it to the EP (which can then communicate with an external program (PC). The electrical interface and Electrode-Tissue interface (c) and (d) illustrate both sensing (1) and stimulation (2) circuit models.

The IPG consumes 20 mW when running autonomously in Therapy Delivery mode (and slightly more when sending data to the EP). Taking into account the ~50% power delivery efficiency of the inductive link, the total power consumption of the system is 40 mW, within the range of commercially available cochlear implants (e.g., 20 mW to 100 mW for the Cochlear Nucleus 7 [27]). The EP can support more than 8-hours of use per charge with a 210mAh Lithium-ion battery, and we expect battery life to significantly increase over time with improved battery technologies and system efficiencies. For our forthcoming clinical study, we plan to provide patients with a second EP device to support 16 h per day of therapy delivery.

Preclinical ovine study

To evaluate the performance of the Smart Neurostimulation System (SNS), we conducted a preclinical study using an ovine model. Fig. 5 outlines the study design. After receiving approval from the NAMSA Institutional Animal Care and Use Committee (IACUC), we performed CT imaging to guide trajectory planning for electrode implantation. On Day 0, a functional neurosurgeon (R.E.G. or B.C.L.) implanted a single SNS IPG and two depth leads per animal, followed by post-operative CT scans to confirm lead placement. Each animal was allowed a six-day recovery period before initiating neural recordings and stimulation.

The IPG was designed for installation into the human cranium. However, anatomical constraints prevent installation in the sheep cranium. Therefore, the IPG was installed in the neck of the animal, housed in an exoskeleton that protected the IPG coil from large flexion forces during movement, which could damage the IPG.

Animals were housed under veterinary supervision with free movement within their enclosures throughout the study. At the study's conclusion, each animal was humanely euthanized. Table 1 summarizes the characteristics of each animal and the implanted devices.

To localize the electrodes anatomically, we registered post-operative CT scans to the Turone sheep brain MRI atlas [28,29] using ITK-SNAP. The iterative metal artifact reduction (iMAR) algorithm was applied to reduce CT signal distortion from the electrodes. We used bright metal artifacts to identify electrode positions and extracted 3D coordinates

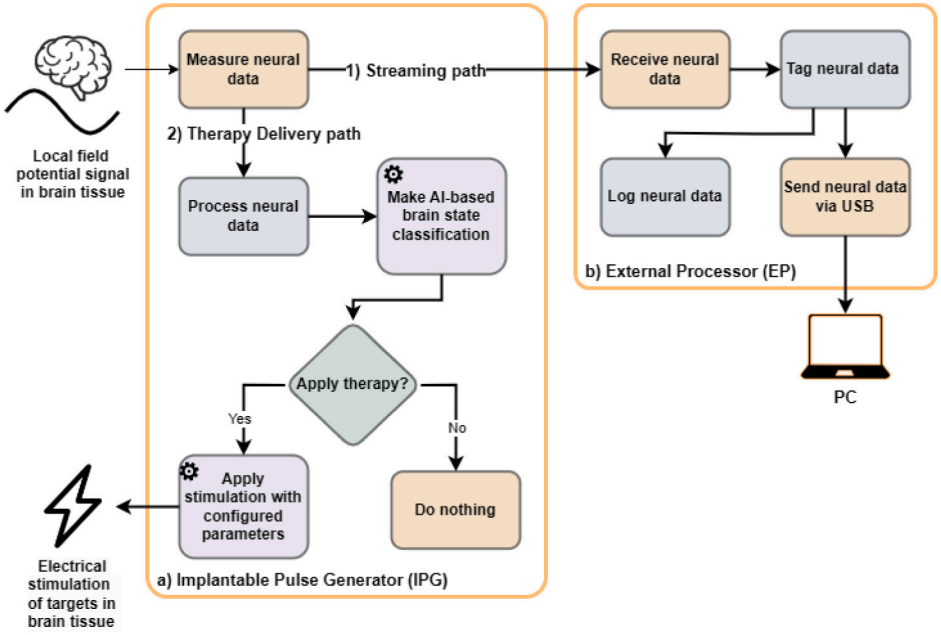

Fig. 4. SNS firmware overview. The SNS includes firmware running on both the IPG (a) and the External Processor (b) to sense neural data and administer electrical stimulation. Once it is sensed from the brain, neural data can take two paths (numbered): (1) a Streaming path where data is sent to an external computer via USB; and (2) a Therapy Delivery path where the data are processed and therapy is administered based on brain state classification. Brain state classification and therapy delivery blocks are programmable and adaptable (marked with a gear icon).

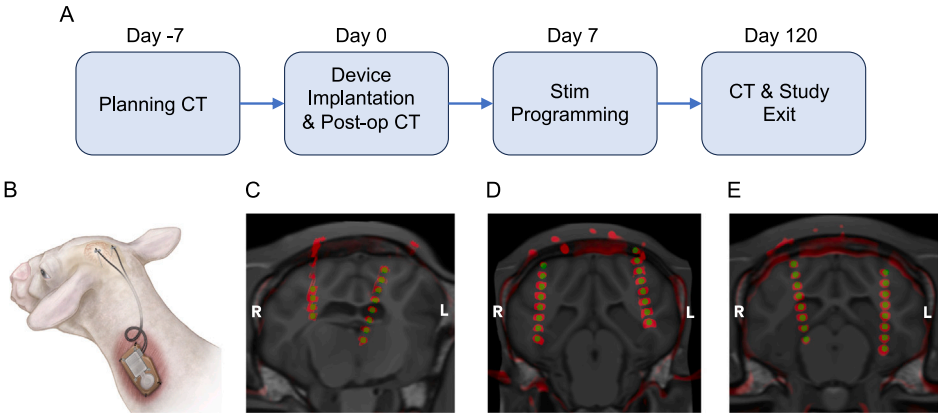

Fig. 5. Preclinical study design and surgical approach. (A) Time course of the preclinical study. CT imaging was collected on Day -7, Day 0 (post-implantation) and Day 120 (prior to study exit). (B) The IPG and a protective exoskeleton were implanted into a pocket in the neck, and two leads were implanted into the left and right parietal lobes. A prelinical EP device bandaged on the skin overlying the IPG coil (not shown) communicated with and powered the IPG. (C, D, E) CT imaging showing the locations of the depth leads in animals S001, S002 and S003, respectively.

relative to anatomical regions defined by the atlas. Table 2 reports the anatomical locations for all monopolar electrodes.

Each SNS lead included eight channels, numbered with even integers from 2 to 16. Channel 8 served as the sensing reference, and all reference electrodes were internally connected within the IPG. (The commercial control lead did not include a reference electrode and thus did not contribute to the reference scheme in animal 1.) For analysis, we generated bipolar "virtual" recordings by subtracting voltages between adjacent non-reference electrodes (e.g., A2–A4). Bipolar referencing, computed as the voltage difference between pairs of adjacent electrodes, filters out signals common to both channels, thereby improving signal-to-noise ratio. This referencing scheme attenuates oculomotor and electromyographic artifacts that can mix with neural signals, and large-N human studies have shown that bipolar referencing of intraparenchymal electrodes better resolves the neural correlates of memory than average referencing [30]. On each SNS lead, the fourth most distal electrode (denoted number eight) served as the electrical reference for the other electrodes. We developed a small computing system (based on a Raspberry Pi processor) to collect data from the preclinical EP and store it on SD cards for subsequent offline analyses, described below.

All three animals underwent surgical implantation without intraoperative complications. The most commonly observed adverse effect was localized swelling at the IPG site, which resolved with pressure bandaging. Routine veterinary assessments confirmed normal wound healing, and there was no evidence of infection, hemorrhage, or tissue damage at the lead implantation sites. One serious adverse event occurred in Animal 3: erosion of the skin overlying the IPG coil. This was attributed to an EP redesign intended to improve its physical robustness that reduced the coil surface area and increased the coil magnetic force, unintentionally increasing the skin pressure beyond the safe limit of 3.7 kPa [31]. We have since decreased the EP magnet strength to keep skin pressure below the safe limit.

Table 2
Monopolar electrode locations. Labels A and B refer to Nia eight-channel leads implanted in the left and right hemispheres, respectively; Label M refers to the Medtronic control lead implanted in S001. Localization methods appear in the text.

Subject	Electrode label	X	Y	Z	Hemisphere	Anatomical label
S001	A2	−0.5	5.5	2	L	Nucleus intermediodorsalis
	A4	−1.75	5.5	6	L	Nucleus habenulae
	A6	−2.75	5.5	8.75	L	Fornix
	A8	−4	6	12	L	Lateral ventricle
	A10	−5	6	15.25	L	White matter bundle
	A12	−6	6	18.25	L	Lateral gyrus
	A14	−6.75	6.25	21.5	L	White matter bundle
	A16	−8	6.25	25	L	White matter bundle
	M1	13.25	−1.25	10	R	White matter bundle
	M2	13.75	−1.25	12.5	R	Caudate
	M3	14.25	−1.25	15.25	R	White matter bundle
S002	A2	−19.25	−2.5	−31.75	L	White matter bundle
	A4	−18.5	−2.5	−28.25	L	White matter bundle
	A6	−18	−2.5	−24.75	L	Suprasylvius gyrus
	A8	−17.25	−2.5	−21.25	L	Suprasylvius gyrus
	A10	−16.75	−2.5	−18	L	White matter bundle
	A12	−16.25	−2.5	−14.75	L	Suprasylvius gyrus
	A14	−15.5	−2.5	−11	L	Suprasylvius gyrus
	A16	−14.75	−2.5	−7.75	L	Skull
	B2	18.5	−2.5	−37.25	R	Temporal gyrus
	B4	18.25	−2.5	−33.75	R	White matter bundle
	B6	17.75	−2.5	−30	R	white matter bundle
	B8	17.5	−2.5	−26.5	R	Posterior sylvian gyrus
	B10	17	−2.5	−23	R	White matter bundle
	B12	17.25	−2.5	−19.25	R	White matter bundle
	B14	16.75	−2.5	−15.75	R	White matter bundle
	B16	16.25	−2.5	−12.75	R	Suprasylvius gyrus
S003	A2	−16	−3.25	−3	L	Parahippocampal cortex
	A4	−16	−3.25	0.25	L	Hippocampus
	A6	−16	−3.25	3.75	L	Hippocampus
	A8	−16.25	−3.25	7.5	L	White matter bundle
	A10	−16.25	−3.25	10.75	L	White matter bundle
	A12	−16.5	−3.25	14.25	L	White matter bundle
	A14	−16.25	−3.25	17.75	L	White matter bundle
	A16	−16	−3.25	21.25	L	Suprasylvius gyrus
	B2	9.5	−3.25	0	R	White matter bundle
	B4	10	−3.25	3.25	R	White matter bundle
	B6	10.5	−3.25	6.75	R	Hippocampus
	B8	11.25	−3.25	10.25	R	Hippocampus
	B10	11.75	−3.25	13.75	R	White matter bundle
	B12	12.25	−3.25	17.25	R	White matter bundle
	B14	13	−3.25	20.5	R	White matter bundle
	B16	13.5	−3.25	24	R	Ectolateral gyrus

Using neural recordings to predict movement

We first asked whether the SNS could record and decode neural signals related to animal behavior. With a triaxial accelerometer sampling at 10 Hz, we gauged the animal's activity level throughout two-hour sessions. We selected non-overlapping 1-second epochs from longer sustained periods of movement or stillness, and used the neural data from these epochs to classify movement in hold-out sessions. Whenever an accelerometer reading exceeded $0.03\ \mathrm{m/s^2}$, and more than 30% of samples in the following 10 s exceeded the accelerometer threshold, we created a "movement" epoch. Whenever an accelerometer reading was below $0.03\ \mathrm{m/s^2}$, if all samples in the prior 60 and subsequent 15 s were below the threshold, we created a "stillness" epoch. We included sessions that had at least 100 movement and 100 stillness epochs, and neither class made up more than 80% of the total epochs.

The final dataset comprised 48, 36, and 48 sessions from the three sheep, respectively. For each one-second epoch, we calculated the spectral powers using Morlet wavelets at eight log-spaced frequencies, ranging from 6 to 180 Hz. The powers were then log-transformed and z-scored within each recording channel and frequency, and then averaged across the one-second epoch. The spectral powers for every epoch at each frequency and channel served as the features input to an L^2-penalized logistic regression classifier, where the labels indicated the movement or stillness identity of each epoch. Using an 80–20 session split, we trained the classifiers to discriminate brain activity predictive of movement and stillness. For cross-validation, we randomly repeated the 80–20 session split, with the number of permutations equal to the number of sessions. We computed the area under the receiver operating characteristic curve (AUC) to quantify classifier performance for each permutation.

Fig. 6A demonstrates the cross-validation in an example session. Accelerometer readings, in cyan, suggest the animal exhibited two periods of reliable stillness and two periods of significant activity. Red and blue dots indicate classifier outputs for epochs labeled as "movement" and "stillness", respectively. Blue dots tend to fall under the 0.5 classifier output threshold, and red dots tend to stay above it, indicating that classifier predictions agreed with the accelerometer reading interpretations in most cases.

We illustrate receiver operating characteristic (ROC) curves in Fig. 6B. For each animal, the hit rate rises quickly towards 1.0 as the false alarm rate increases, suggesting neural features reliably classify the animal's activity in holdout data. Across the cross-validation test partitions, we found AUC values of ($M = 0.924, SD = 0.031$), ($M = 0.979, SD = 0.008$), and ($M = 0.969, SD = 0.008$) for the three sheep. As a control analysis, we repeated the cross-validation with shuffled movement/stillness labels for the training and test data, finding AUC values of ($M = 0.500, SD = 0.005$), ($M = 0.502, SD = 0.006$), and ($M = 0.499, SD = 0.005$). We also trained movement classifiers for

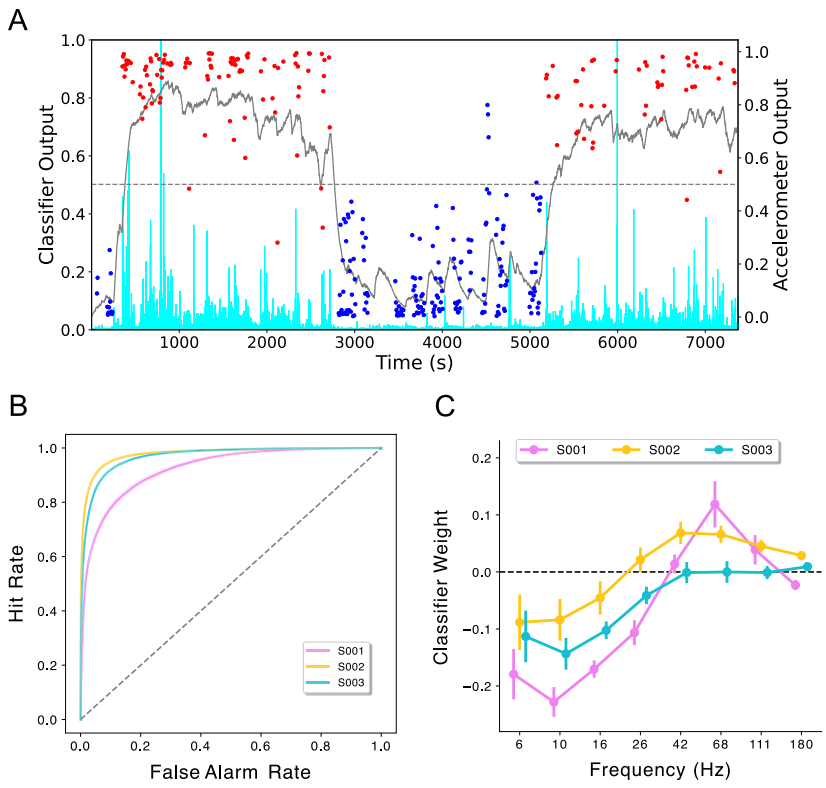

Fig. 6. Classification of animal movement. (A) We trained an L2 logistic regression classifier to predict periods of movement vs. stillness based on spectral features. Across a two-hour hold-out session, we show that classifier output probability (gray) tracks periods of movement (red) and stillness (blue). These representative periods were chosen based on the accelerometer magnitude readings (cyan) sampled at 10 Hz and high-pass filtered with a cutoff at 0.1 Hz. (B) A ROC analysis, which shows the relation between true and false positives as a function of decision criterion, quantifies classifier performance. (C) The Haufe method reveals the degree of influence of different features on classification performance while adjusting for the covariance structure in the model. Here we see that increased weights on high frequencies and decreased weights on low frequencies predicted movement. Error bars represent one standard error of the mean across recording channels.

each animal on data from the first half of the study and tested these classifiers on data from each week within the second half of the study. We found that classifiers generalized very well from the first half to the second half of the study, with average AUCs of 0.929 (SD = 0.013), 0.962 (SD = 0.038), and 0.973 (SD = 0.011), for the three animals. These findings demonstrate the stability of the SNS' neural recordings and classifier weights across many weeks of recordings.

Previous analyses of neural data during motor tasks have identified increases in high-frequency power (>30 Hz) and decreases in low-frequency power [19] during and immediately preceding movement. To determine whether our classifier uncovered similar neural correlates of movement, we applied the Haufe method [32] to the weights obtained from the optimal classifier fit to cross-validation training datasets. This method transforms classifier weights to account for the covariances between features. In Fig. 6C, we illustrate that increased high-frequency power and decreased low-frequency power tended to mark high activity periods. Although aggregating across all electrodes illustrated a similar trend across animals, the classifiers identified the unique pattern of neural activity related to behavior within each animal.

Neural recordings and stimulation performance

To evaluate the SNS's ability to modulate neural activity, we ran two stimulation experiments. We compared spectral power in the 200–950 ms post-stimulation period to power in the −750–0 ms pre-stimulation period. Analyzing the post-stimulation period, isolated stimulation induced brain activity that persists beyond the stimulation interval, and the 200-ms post-stimulation buffer attenuated potential stimulation artifact. Guided by prior work on spectral biomarkers of cognition, we focused on alpha (8–12 Hz) and gamma (78–82 Hz) band power. We used Welch's method to calculate the power spectral densities during the pre- and post-stimulation periods, which does not require a buffer that risks leakage from the stimulation period. Before further analysis, we log-transformed each power value, as in previous work [19,33], and calculated the z-scores of spectral powers within each frequency, channel, and session. For every stimulation event, i, within each frequency, f, and channel, c, we computed the difference in post- and pre-stimulation power as $\Delta_{\mathrm{P(f,c,i)}} = \mathrm{P(f,c,i)}_{post} - \mathrm{P(f,c,i)}_{pre}$ (Fig. 7C).

Parameter search: Experiment 1

Experiment 1, conducted on S001, tested whether the SNS could reliably modulate neural activity. Applying stimulation at varying amplitudes and frequencies at a single pair of neighboring electrodes, we evaluated power changes at the remaining non-anode, non-cathode electrodes on the same implanted lead. On each trial, the SNS applied 300 μs biphasic stimulation pulses at frequencies of 25, 50, 100 and 200 Hz and amplitudes of 0 (sham), 0.2, 0.4, 0.6, 0.8, and 1 mA across a bipolar pair of neighboring electrodes ($A10-A12$) in left frontal white matter (Fig. 5C). To minimize order effects, we shuffled stimulation *trials* to create 10 uniquely ordered session protocols, each with 30 trials of each of the 24 frequency × amplitude combinations. Each trial applied stimulation for 500 ms, followed by a 2.0–2.25 s inter-trial interval (Fig. 7A). One sheep completed 124 sessions.

Increasing stimulation amplitude and frequency boosted both alpha and gamma power (Fig. 8). These effects broadly align with prior

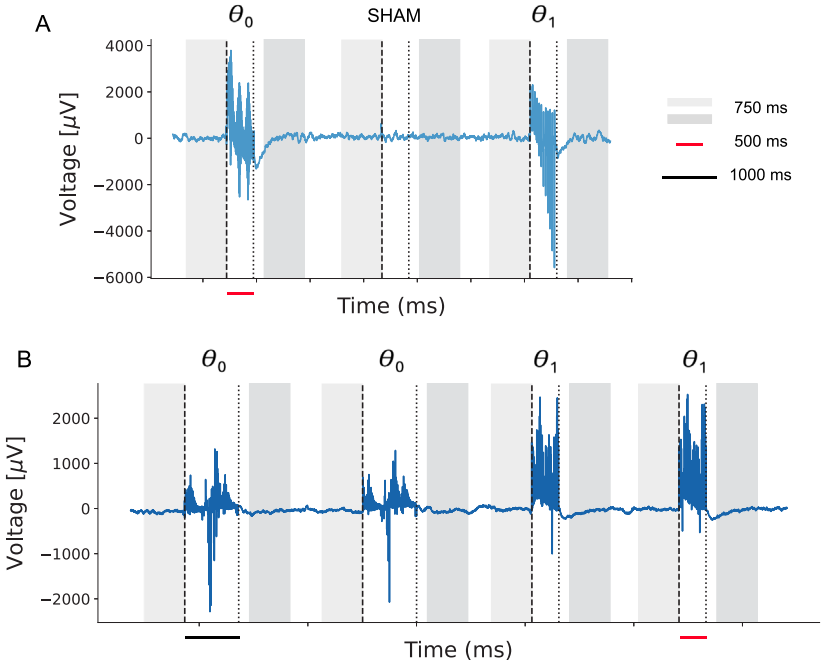

Fig. 7. Parameter search methods. We applied stimulation with varying parameter sets θ and analyzed spectral powers from −750 to 0 ms (light gray) before stimulation onset (dashed line) and 200 to 950 ms (dark gray) following stimulation offset (dotted line). (A) In Experiment 1, the SNS delivered 500 ms bi-phasic stimulation bursts at varying amplitudes [Sham, 0.2, 0.4, 0.6, 0.8, 1 mA] and frequencies [f = 25, 50, 100 and 200 Hz] at a single target location (A10-A12), with the parameter set updating each stimulation event. Example field potential recorded from a bipolar electrode pair (A14-A16). (B) In Experiment 2, the SNS delivered bi-phasic stimulation bursts at varying amplitudes [0.5, 1, 1.5 mA], frequencies [100, 200 Hz], and durations [500, 1000 ms] at twelve target locations, with the parameter set updating every two stimulation events. Example field potential recorded from a bipolar electrode pair (B4-B6).

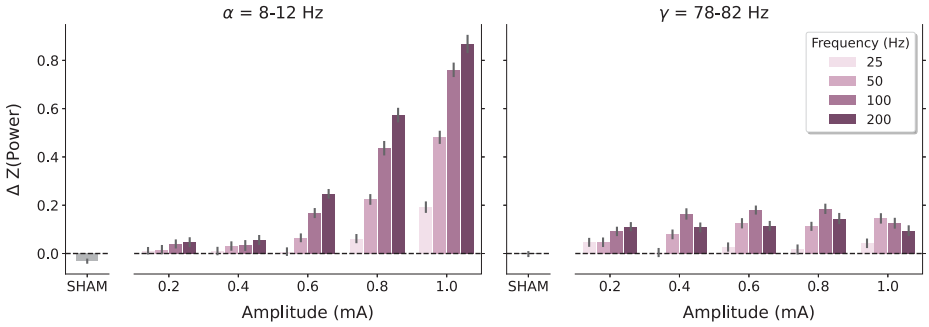

Fig. 8. Stimulation's physiological effects: Experiment 1. The effect of stimulation amplitude and frequency on alpha-band power (8–12 Hz, left panel) and gamma-band power (78–82 Hz, right panel). This analysis averages over the three electrode pairs that do not overlap with either the anode or cathode. Increasing stimulation amplitude and frequency results in greater power increases.

stimulation parameter search experiments in humans [34]. We evaluated these trends with a linear mixed effects model containing fixed effects for stimulation amplitude, frequency, and their interaction, a random intercept for session, and had predictor variables centered and normalized to the range −1 to 1. Our model identified statistically significant linear effects of both stimulation amplitude $\beta = 0.311, CI = [0.303, 0.319]$ and frequency, $\beta = 0.140, CI = [0.134, 0.147]$ on stimulation-related changes in alpha power. Our model also identified a significant interaction between amplitude and frequency, $\beta = 0.159, CI = [0.149, 0.168]$, as seen in the increasing strength of the amplitude-power relation for increasing stimulation frequency evident in Fig. 8. We observe significant relations of stimulation amplitude, $\beta = 0.013, CI = [0.005, 0.022]$, frequency, $\beta = 0.032, CI = [0.025, 0.040]$, and their interaction, $\beta = -0.011, CI = [-0.022, -0.001]$, with changes in gamma power. These results align with previous work finding post-stimulation increases in high-frequency activity (HFA) [34]. Prior research has shown that HFA increases correlate with increases in neural firing rate, linking stimulation-related spectral changes to the modulation of neural activity [35].

Parameter search: Experiment 2

Experiment 2 further explored the modulatory capabilities of the SNS. In two animals (S002 and S003), we stimulated 12 neighboring electrode pairs with varying amplitude, frequency, and duration. We evaluated stimulation's effects on power at the remaining electrodes on the same implanted lead not involved in stimulation and the electrodes on the other implanted lead. On each trial, the SNS applied 300 μs biphasic stimulation pulses at frequencies of 100 and 200 Hz, amplitudes of 0.5, 1, and 1.5 mA, and durations of 500 and 1000 ms. As illustrated in Fig. 7B, stimulation trials occurred in blocks of two stimulation events with the same stimulation parameters. Within a block, the two stimulation events occurred with a random inter-trial interval of either 1000–1250 ms or 2000–2250 ms. Across blocks, there

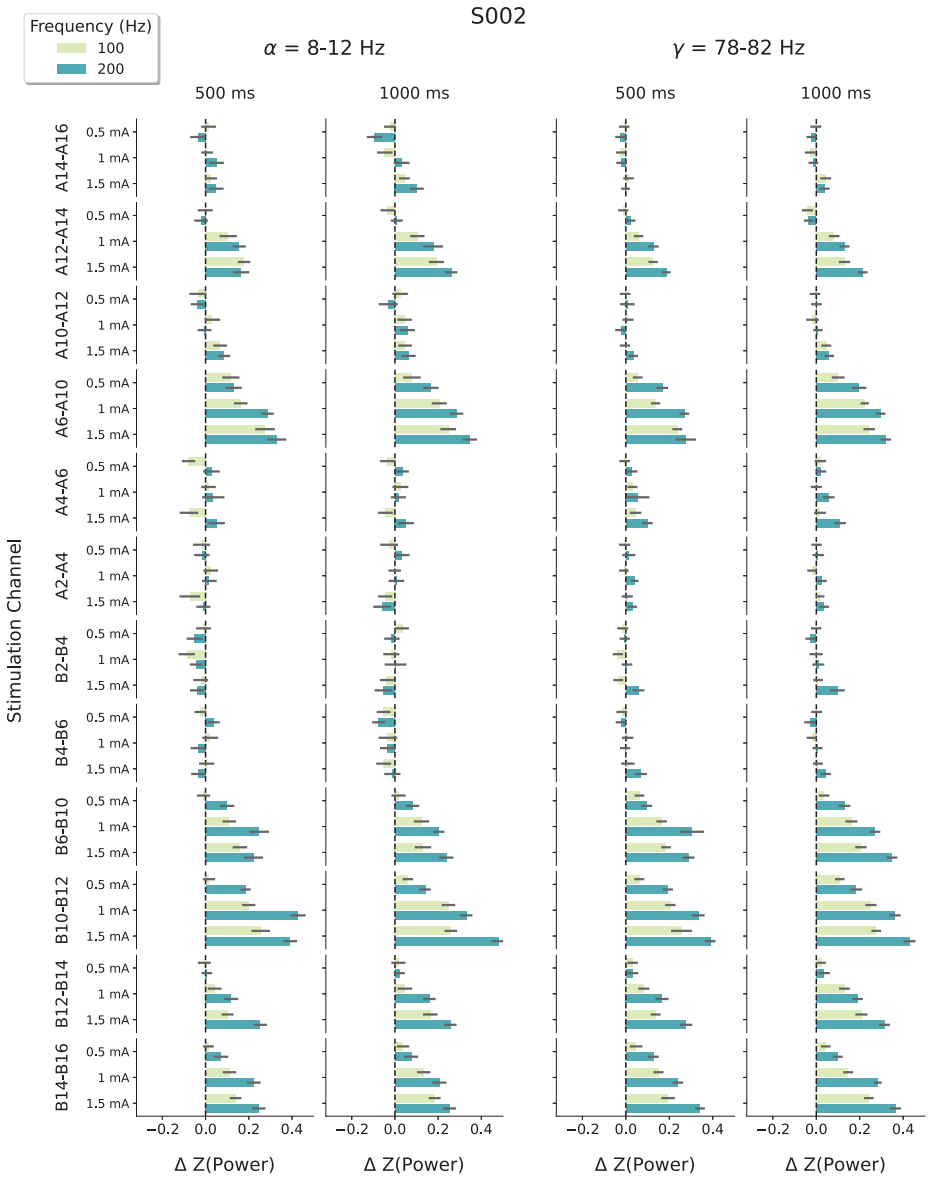

Fig. 9. Stimulation's physiological effects: Experiment 2. The effect of stimulation amplitude, frequency, duration, and location on alpha-band power (8–12 Hz, left panel) and gamma-band power (78–82 Hz, right panel) for animal S002. This analysis averages over the nine electrode pairs that do not overlap with either the anode or cathode. The effects of the stimulation parameters depend greatly on the location of stimulation.

was a random 2000–2250 ms inter-stimulus interval. We collected a total of 42 and 154 sessions from the two sheep, respectively.

Figs. 9–10 reveal considerable site-to-site heterogeneity in the effects of stimulation amplitude, frequency, and duration on alpha and gamma. This site-to-site variability aligns with stimulation parameter search studies conducted in humans [34]. Overall, stimulation-related power increases appeared far more prevalent than power decreases. To evaluate these effects, we fit linear mixed-effects models for each stimulation location in each animal (fixed effects: amplitude, frequency, duration, and pairwise interactions; random intercept for session; with predictors centered and normalized in Experiment 1). We FDR corrected across the parameters estimated within each subject and frequency band [36]. For some stimulation locations (e.g., B10-B12 in both animals), increasing stimulation amplitude and frequency led to greater increases in both alpha and gamma power (all $t > 8$ and all $p < 0.001$), mirroring Experiment 1. However, at other sites, we observe no effect of amplitude (e.g., A2-A4 in animal S002) or frequency (e.g., A4-A6 in animal S003) on alpha or gamma power. In some cases, we observe negative effects of amplitude (e.g., B4-B6 in animal S003, alpha and gamma power, both $t < -4.0$ and $p < 0.001$) but we observe no negative effects of frequency.

Fig. 11 summarizes the modeling results. More than half of all stimulation targets increased alpha and gamma power, and only two consistently decreased alpha power. Increasing stimulation amplitude tended to consistently increase post-stimulation changes in alpha and gamma; however, we did observe a small number of locations where changes in power decreased with increasing amplitude. Stimulation frequency exhibited a similar pattern to stimulation amplitude. We detected many fewer stimulation locations where duration reliably modulated either alpha or gamma power, and those locations did not show a clear directional pattern. The pairwise interactions between amplitude, frequency, and duration exhibited a diversity of results, mirroring that seen in Figs. 9 and 10.

Closed loop modulation of spectral power

After demonstrating the system's capacity to record and decode neural signals and modulate spectral features with electrical stimulation,

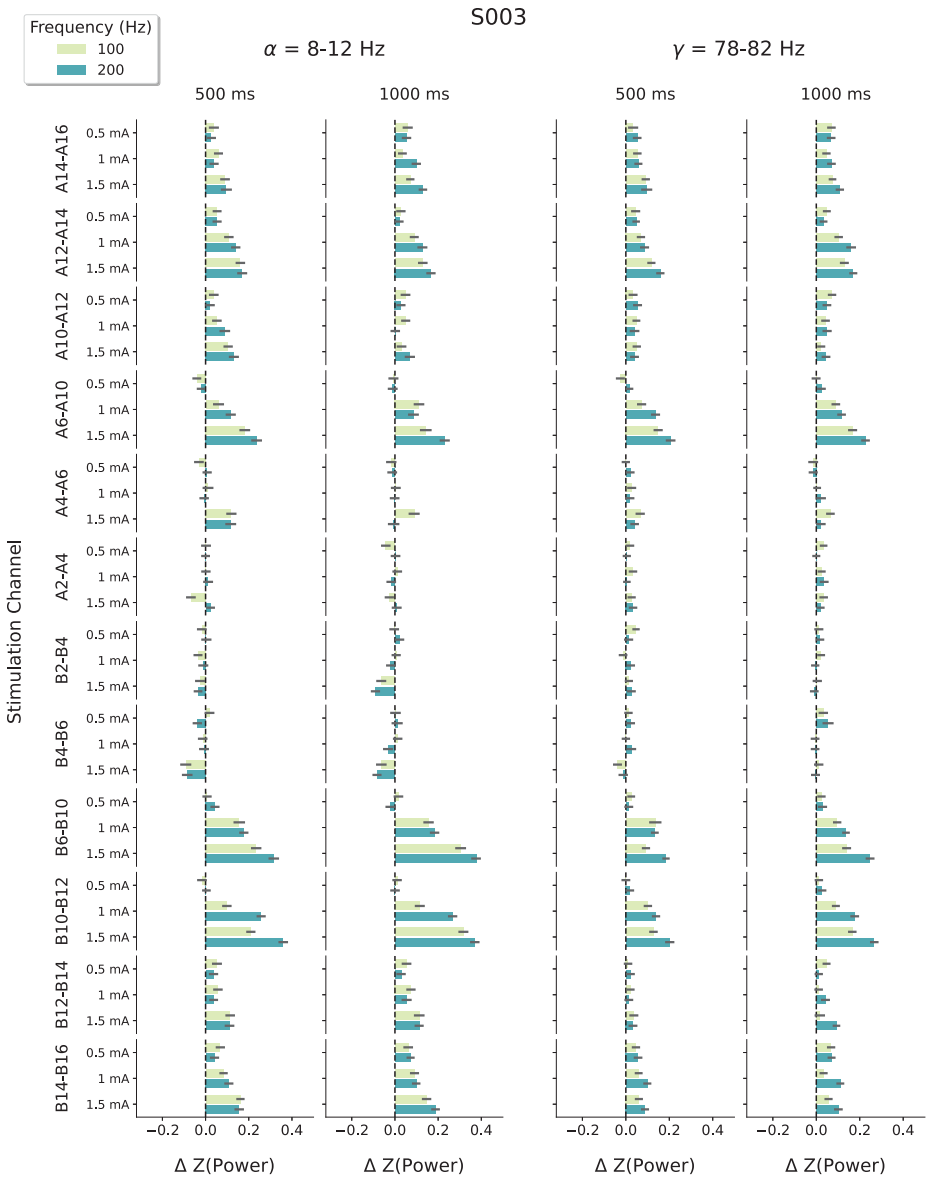

Fig. 10. Stimulation's physiological effects: Experiment 2. The effect of stimulation amplitude, frequency, duration, and location on alpha-band power (8–12 Hz, left panel) and gamma-band power (78–82 Hz, right panel) for animal S003. This analysis averages over the nine electrode pairs that do not overlap with either the anode or cathode. The effects of the stimulation parameters depend greatly on the location of stimulation.

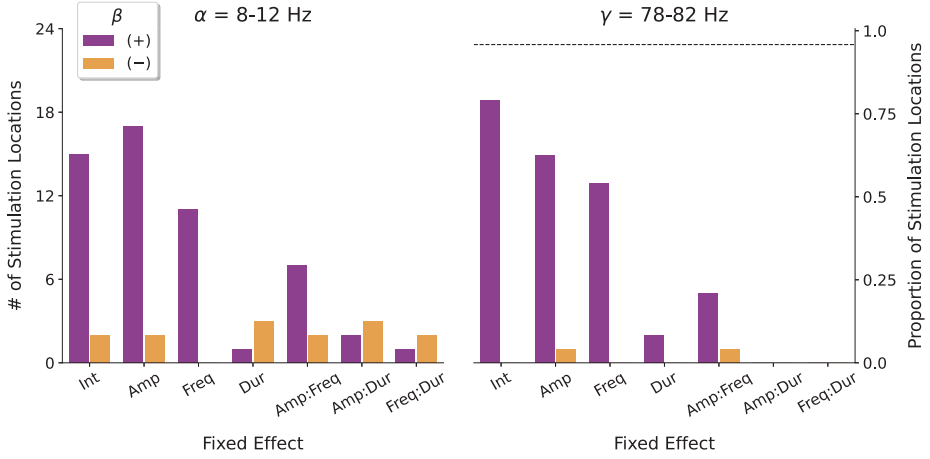

Fig. 11. Linear mixed effects modeling of stimulation parameters. Number of stimulation targets exhibiting significant effects of stimulation amplitude, frequency, duration (and all pairwise interactions) on changes in alpha- and gamma-band power. Aggregated data from animals S002 and S003.

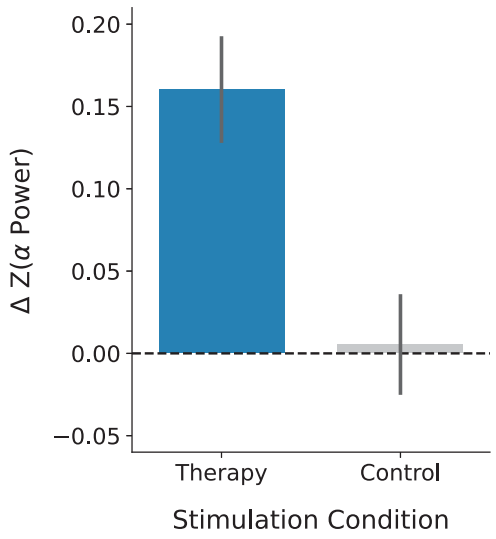

Fig. 12. Closed-loop alpha power modulation. Stimulation during periods of low alpha-power with a therapy parameter set reliably increased alpha-power, while a control parameter set did not modulate alpha-power. Error bars represent one standard error of the mean around average modulations from 57 sessions.

we tested its ability to perform these tasks in real time for closed-loop functionality. For S002, we selected a "therapy" stimulation parameter set from the parameter search data (θ_T) that reliably increased alpha-power and a "control" stimulation parameter set (θ_C) that did not change alpha-power. When the SNS detected low alpha-power (below the average value), we either stimulated with θ_T or θ_C and evaluated the subsequent changes in alpha-power. Fig. 12 illustrates that stimulation with the therapy parameter increased alpha-power in closed-loop; no such increase appeared for the control parameter set.

Brain histology

We performed histopathology on brain tissue proximal to the implanted depth leads in all three animals. In brief, we fixated the brain, trimmed the region of interest, embedded it in paraffin, sectioned, and stained it with hematoxylin and eosin, Luxol Fast Blue (LFB) for demyelination, Glial Fibrillary Acidic Protein for astrocytosis, IBA-1 to identify macrophages and microglia, and Fluro Jade B (FJB) to evaluate neuronal necrosis. (FJB staining was performed in Animal 1 only.) The study pathologist utilized light microscopy to examine stained sections and assessed them based on predefined histological evaluation criteria for cellular and tissue response.

No indicators of severe inflammatory response or damage were observed in any brain sections examined: (1) Inflammatory Cells: Polymorphonuclear cells, lymphocytes, multinucleated giant cells, and plasma cells (Score 0); and (2) Necrosis (Score 0). Observed changes in the primary brain tissue were consistent with minor injury resulting from the implant procedure itself: (1) Astrocytosis, defined as gliosis, was present, generally ranging from minimal to mild; (2) Expression of Iba-1, a marker for Microglia/Macrophage / Gitter Cells, ranged from minimal to moderate. (3) Demyelination was absent in nearly all sections examined across all three animals. (4) Neovascularization and Fibrosis were either absent or minimal (Score 1) in limited regions. In S001, which had the SNS Depth Lead implanted into the left hemisphere and a Control Lead implanted into the right hemisphere, we observed no significant differences in tissue response between the implanted brain hemispheres.

While glial encapsulation of electrode arrays represents a concern for BCI systems that record single- or multi-unit activity using high-impedance (~100 kΩ) micro-electrodes with a small surface area (~0.001 mm^2), the SNS records local field potentials using low-impedance (<100 Ω) macro-electrodes with a relatively large (5.3 mm^2) surface area. These local field potentials are relatively immune to signal-to-noise changes due to glial encapsulation, as evidenced by the Neuropace RNS device, which utilizes a similar electrode design to treat epilepsy using closed-loop neurostimulation and has demonstrated efficacy for more than nine years in many patients [37].

Discussion

Brain-responsive stimulation now represents an established therapy for epilepsy and movement disorders, with promise for treating chronic pain, depression, and other conditions [2–6,38]. However, FDA-cleared platforms only decode a single spectral feature from a handful of channels. The Smart Neurostimulation System (SNS) overcomes this limitation by measuring electrical fields across 60 bipolar contacts on four depth leads and providing embedded algorithms for spectral processing and classifier-based stimulation control.

The ability to stimulate the brain in response to distributed patterns of neural activity may be particularly useful for neurocognitive and affective disorders where functional impairments vary dramatically from moment to moment [39]. As proof-of-concept, Ezzyat and colleagues [9,12,13] deployed a closed-loop algorithm on a partially externalized device, showing that stimulating the lateral temporal cortex during predicted memory lapses produced significant memory improvements in sham-controlled, double-blinded studies of neurosurgical epilepsy patients. By training logistic regression classifiers on spectral activity during learning, these studies could reliably predict which items would be recalled or forgotten, then trigger stimulation during predicted memory lapses. Mnemonic benefits only appeared for closed-loop stimulation — random stimulation did not improve memory.

We designed the SNS to deliver closed-loop stimulation chronically via an AI-enabled brain implant (IPG) that communicates wirelessly with an external processor (EP). The EP, modeled on a cochlear implant sound processor, delivers power inductively to the IPG and acts as a communication hub with the cloud-based AI platform. Clinical programmer software enables patient-specific models to trigger therapeutic stimulation based on real-time brain state variability. In memory applications, predicted memory lapses will trigger stimulation, and post-minus-prestimulation classifier output will guide stimulation parameter optimization.

Comparison with existing systems

The NeuroPace RNS serves as the closest predicate to the SNS. Both systems record field potentials and stimulate the brain in closed loop with onboard signal processing. However, the RNS records from a maximum of six channels in two brain regions vs. the SNS's 60 channels across four regions. Because seizures often localize to small brain regions, six channels significantly reduce seizures in many patients. However, memory-related brain signals occur across distributed networks [10,11], requiring the widespread surveillance capabilities of the SNS and the ability to adaptively select among a larger set of stimulation targets. Analyses of large open-data sets [21,40] informed the SNS design by identifying whole-brain patterns of neural activity that signal periods of good and poor memory.

The FDA cleared the Medtronic *Percept* adaptive DBS system for Parkinson's disease in 2025. Percept records field potentials from each segmented STN or GPi lead, extracts a single β-band (13–30 Hz) power estimate once per second, and automatically raises or lowers stimulation amplitude when that biomarker crosses clinician-defined thresholds [2,41]. In the pivotal trial, the algorithm maintained motor benefit while significantly reducing delivered charge. Despite these gains,

Table 3
Comparison of BCI systems. Abbreviations: A/Sym = A/symmetric. s.w. = square wave. FFT = Fast Fourier Transform. IIR = Infinite Impulse Response. Stim. Lat. = Stimulation Latency. Data sources: Neuropace RNS [42–44], Medtronic Percept [45,46], Cortec BIC [47,48], Stentrode [49,50], and Neuralink Telepathy [51,52].

Feature	Nia SNS	Neuropace RNS	Medtronic percept	Cortec BIC	Synchron stentrode	Neuralink telepathy
Num. Leads	4	2	2	Varies	1	96 'threads'
Sense channels	60	4	6	32	16	1024
Stim channels	60	8	16	32	0	Unknown
Sampling rate	500 Hz	250 Hz	250 Hz	1000 Hz	2048 Hz	19,300 Hz
Spectral processing	IIR	Unknown	FFT	IIR	None	IIR
Stimulation waveform	Sym. SW	Sym. SW	Sym. SW	Asym. SW	None	Unknown
Stim. lat.	<25 ms	Unknown	~10 ms	<40 ms	N/A	Unknown
Power	Wireless inductive	Primary cell	Primary cell & rechargeable options	Wireless inductive	Unknown	Rechargeable

Percept senses at most two bipolar channels and reacts to one spectral feature, making it unsuitable for decoding cognition functions whose neural features span widespread frequencies and distributed brain networks.

The Cortec Brain Interchange (BIC) is a research system that does not yet have FDA marketing approval, but deserves close comparison with the SNS. The BIC supports neural data collection and closed loop stimulation delivery, though the analysis of neural data and the closed loop control policy takes place on an external computer rather than on the implanted device. This design tradeoff limits the usability and portability of the BIC, but provides a more flexible and powerful algorithm development environment (see Table 3).

Preclinical validation

Our ovine study validates core SNS functionality. Due to the small sheep brain, we implanted two multi-contact depth leads. Stimulation at a single contact pair demonstrated that increasing amplitude and frequency systematically alter alpha- and gamma-band activity at other recording electrodes. Personalized logistic regression classifiers reliably predicted animal movement in hold-out sessions, demonstrating in vivo that the SNS can detect and modulate behaviorally relevant neural signals. Histological analyses showed no adverse tissue response to either lead type.

Limitations and future design considerations

The ovine model, while valuable for demonstrating device functionality, has translation limitations. The smaller sheep brain necessitated only two shorter depth leads (with only nine bipolar pairs available for recording the effects of stimulation after excluding stimulation-adjacent contacts). Additionally, while our experiments demonstrated reliable decoding of movement and spectral power modulation, we did not exercise the SNS's ability to decode higher-cognitive functions, such as memory or its closed-loop functionality.

Conclusions

The Smart Neurostimulation System (SNS) represents a major advance in neuromodulatory technology, offering simultaneous 60-channel brain activity monitoring with automatically configurable, targeted electrical stimulation based on real-time spectral analysis of neural data. Ovine data demonstrate core functionality. Although designed to evaluate an earlier proof-of-concept therapy for memory loss, the SNS's multi-channel sensing and brain-state-contingent stimulation holds the potential to address a broad range of pathologies that exhibit moment-to-moment fluctuations, such as depression, anxiety, chronic pain, and attention disorders. The platform's ability to record from distributed brain networks while delivering targeted stimulation to deep brain structures provides the foundation for a broad range of personalized, biomarker-guided therapies.

CRediT authorship contribution statement

Daniel S. Rizzuto: Writing – review & editing, Writing – original draft, Supervision, Project administration, Conceptualization. **Haydn G. Herrema:** Writing – review & editing, Writing – original draft, Visualization, Methodology, Formal analysis, Data curation. **Zhe Hu:** Methodology. **Daniil Utin:** Software, Methodology. **Joshua Kahn:** Methodology. **Chris Ho:** Software, Methodology. **Andrew B. Smiles:** Methodology. **Robert E. Gross:** Methodology. **Bradley C. Lega:** Methodology. **Sandhitsu R. Das:** Methodology. **Michael J. Kahana:** Writing – review & editing, Writing – original draft, Supervision, Project administration, Conceptualization, Formal Analysis.

Funding

The Army Medical Research and Development Command funded some activities under MTEC project 20-06-MOM. The views, opinions, and/or findings contained in this material are those of the authors and should not be interpreted as representing the official views or policies of the Department of Defense or the U.S. Government.

Declaration of competing interest

D.S.R. and M.J.K. hold a greater than 5% equity interest in Nia Therapeutics Inc., a company intended to develop and commercialize brain stimulation therapies for memory restoration.

References

[1] Nair DR, Laxer KD, Weber PB, Murro AM, Park YD, Barkley GL, Smith BJ, Gwinn RP, Doherty MJ, Noe KH, Zimmerman RS, Bergey GK, Anderson WS, Heck C, Liu CY, Lee RW, Sadler T, Duckrow RB, Hirsch LJ, Wharen REJ, Tatum W, Srinivasan S, McKhann GM, Agostini MA, Alexopoulos AV, Jobst BC, Roberts DW, Salanova V, Witt TC, Cash SS, Cole AJ, Worrell GA, Lundstrom BN, Edwards JC, Halford JJ, Spencer DC, Ernst L, Skidmore CT, Sperling MR, Miller I, Geller EB, Berg MJ, Fessler AJ, Rutecki P, Goldman AM, Mizrahi EM, Gross RE, Shields DC, Schwartz TH, Labar DR, Fountain NB, Elias WJ, Olejniczak PW, Villemarette-Pittman NR, Eisenschenk S, Roper SN, Boggs JG, Courtney TA, Sun FT, Seale CG, Miller KL, Skarpaas TL, Morrell MJ. Nine-year prospective efficacy and safety of brain-responsive neurostimulation for focal epilepsy. Neurology 2020;95(9):e1244–56. http://dx.doi.org/10.1212/WNL.0000000000010154.

[2] Stanslaski S, Summers RLS, Tonder L, Tan Y, Case M, Raike RS, Morelli N, Herrington TM, Beudel M, Ostrem JL, Little S, Almeida L, Ramirez-Zamora A, Fasano A, Hassell T, Mitchell KT, Moro E, Gostkowski M, Sarangmat N, Bronte-Stewart H. On behalf of the ADAPT-PD investigators, sensing data and methodology from the Adaptive DBS Algorithm for Personalized Therapy in Parkinson's Disease (ADAPT-PD) clinical trial. Npj Parkinson's Dis 2024;10(1):174. http://dx.doi.org/10.1038/s41531-024-00772-5.

[3] Mekhail NA, Levy RM, Deer TR, Kapural L, Li S, Amirdelfan K, Pope JE, Hunter CW, Rosen SM, Costandi SJ, Falowski SM, Burgher AH, Gilmore CA, Qureshi FA, Staats PS, Scowcroft J, McJunkin T, Carlson J, Kim CK, Yang MI, Stauss T, Petersen EA, Hagedorn JM, Rauck R, Kallewaard JW, Baranidharan G, Taylor RS, Poree L, Brounstein D, Duarte RV, Gmel GE, Gorman R, Gould I, Hanson E, Karantonis DM, Khurram A, Leitner A, Mugan D, Obradovic M, Ouyang Z, Parker J, Single P, Soliday N. Ecap-controlled closed-loop versus

open-loop scs for the treatment of chronic pain: 36-month results of the evoke blinded randomized clinical trial. Reg Anesth Pain Med 2024;49(5):346–54. http://dx.doi.org/10.1136/rapm-2023-104751.

[4] Nijhuis H, Kallewaard J-W, van de Minkelis J, Hofsté W-J, Elzinga L, Armstrong P, Gültuna I, Almac E, Baranidharan G, Nikolic S, Gulve A, Vesper J, Dietz BE, Mugan D, Huygen FJPM. Durability of evoked compound action potential (ecap)-controlled, closed-loop spinal cord stimulation (scs) in a real-world european chronic pain population.. Pain Ther 2024;13(5):1119–36. http://dx.doi.org/10.1007/s40122-024-00628-z.

[5] Scangos KW, Khambhati AN, Daly PM, Makhoul GS, Sugrue LP, Zamanian H, Liu TX, Rao VR, Sellers KK, Dawes HE, Starr PA, Krystal AD, Chang EF. Closed-loop neuromodulation in an individual with treatment-resistant depression. Nature Med 2021;27(10):1696–700. http://dx.doi.org/10.1038/s41591-021-01480-w.

[6] Widge AS, Malone DA, Dougherty DD. Closing the loop on deep brain stimulation for treatment-resistant depression. In: Frontiers in neuroscience volume 12-2018. 2018, http://dx.doi.org/10.3389/fnins.2018.00175, URL https://www.frontiersin.org/journals/neuroscience/articles/10.3389/fnins.2018.00175.

[7] Widge AS. Closing the loop in psychiatric deep brain stimulation: physiology, psychometrics, and plasticity.. Neuropsychopharmacology 2024;49(1):138–49. http://dx.doi.org/10.1038/s41386-023-01643-y.

[8] Ezzyat Y, Kragel JE, Burke JF, Levy DF, Lyalenko A, Wanda PA, O'Sullivan L, Hurley KB, Busygin S, Pedisich I, Sperling MR, Worrell GA, Kucewicz MT, Davis KA, Lucas TH, Inman CS, Lega BC, Jobst BC, Sheth SA, Zaghloul K, Jutras MJ, Stein JM, Das SR, Gorniak R, Rizzuto DS, Kahana MJ. Direct brain stimulation modulates encoding states and memory performance in humans. Curr Biol. 2017;27(9):1251–8. http://dx.doi.org/10.1016/j.cub.2017.03.028.

[9] Ezzyat Y, Wanda PA, Levy DF, Kadel A, Aka A, Pedisich I, Sperling MR, Sharan AD, Lega BC, Burks A, Gross RE, Inman CS, Jobst BC, Gorenstein MA, Davis KA, Worrell GA, Kucewicz MT, Stein JM, Gorniak R, Das SR, Rizzuto DS, Kahana MJ. Closed-loop stimulation of temporal cortex rescues functional networks and improves memory. Nat Commun 2018;9(1):365. http://dx.doi.org/10.1038/s41467-017-02753-0, URL https://www.nature.com/articles/s41467-017-02753-0.

[10] Kragel JE, Ezzyat Y, Sperling MR, Gorniak R, Worrell GA, Berry BM, Inman C, Lin J-J, Davis KA, Das SR, Stein JM, Jobst BC, Zaghloul KA, Sheth SA, Rizzuto DS, Kahana MJ. Similar patterns of neural activity predict memory function during encoding and retrieval. NeuroImage 2017;155:60–71. http://dx.doi.org/10.1016/j.neuroimage.2017.03.042, URL https://linkinghub.elsevier.com/retrieve/pii/S1053811917302549.

[11] Weidemann CT, Kragel JE, Lega BC, Worrell GA, Sperling MR, Sharan AD, Jobst BC, Khadjevand F, Davis KA, Wanda PA, Kadel A, Rizzuto DS, Kahana MJ. Neural activity reveals interactions between episodic and semantic memory systems during retrieval. 148, (1):2019, p. 1–12. http://dx.doi.org/10.1037/xge0000480, URL https://doi.apa.org/doi/10.1037/xge0000480.

[12] Kahana MJ, Ezzyat Y, Wanda PA, Solomon EA, Adamovich-Zeitlin R, Lega BC, Jobst BC, Gross RE, Ding K, Diaz-Arrastia RR. Biomarker-guided neuromodulation aids memory in traumatic brain injury. Brain Stimul 2023;16(4):1086–93. http://dx.doi.org/10.1016/j.brs.2023.07.002, URL https://linkinghub.elsevier.com/retrieve/pii/S1935861X23018168.

[13] Ezzyat Y, Kragel JE, Solomon EA, Lega BC, Aronson JP, Jobst BC, Gross RE, Sperling MR, Worrell GA, Sheth SA, Wanda PA, Rizzuto DS, Kahana MJ. Functional and anatomical connectivity predict brain stimulation's mnemonic effects. Cerebral Cortex 2023;34(1):bhad427. http://dx.doi.org/10.1093/cercor/bhad427, URL https://academic.oup.com/cercor/article/doi/10.1093/cercor/bhad427/7457341.

[14] Kahana MJ, Aggarwal EV, Phan TD. The variability puzzle in human memory. J Exp Psychol [Learn Mem Cogn] 2018;44(12):1857–63. http://dx.doi.org/10.1037/xlm0000553.

[15] Rubinstein DY, Weidemann CT, Sperling MR, Kahana MJ. Direct brain recordings suggest a causal subsequent-memory effect. Cerebral Cortex 2023;33(11):6891–901. http://dx.doi.org/10.1093/cercor/bhad008, URL https://academic.oup.com/cercor/article/33/11/6891/7005169.

[16] Bercaw EL, Hanks RA, Millis SR, Gola TJ. Changes in neuropsychological performance after traumatic brain injury from inpatient rehabilitation to 1-year follow-up in predicting 2-year functional outcomes. Clin Neuropsychol 2011;25(1):72–89. http://dx.doi.org/10.1080/13854046.2010.532813.

[17] Cifu DX, Keyser-Marcus L, Lopez E, Wehman P, Kreutzer JS, Englander J, High W. Acute predictors of successful return to work 1 year after traumatic brain injury: A multicenter analysis. Arch Phys Med Rehabil 1997;78(2):125–31. http://dx.doi.org/10.1016/S0003-9993(97)90252-5.

[18] Goertzel G. An algorithm for the evaluation of finite trigonometric series. Am Math Mon 1958;65:34–5.

[19] Burke JF, Ramayya AG, Kahana MJ. Human intracranial high-frequency activity during memory processing: neural oscillations or stochastic volatility? Curr Opin Neurobiol 2015;31:104–10. http://dx.doi.org/10.1016/j.conb.2014.09.003, URL https://linkinghub.elsevier.com/retrieve/pii/S0959438814001810.

[20] Greenberg JA, Burke JF, Haque R, Kahana MJ, Zaghloul KA. Decreases in theta and increases in high frequency activity underlie associative memory encoding.. NeuroImage 2015;114:257–63. http://dx.doi.org/10.1016/j.neuroimage.2015.03.077.

[21] Rahimzadeh V, Jones KM, Majumder MA, Kahana MJ, Rutishauser U, Williams ZM, Cash SS, Paulk AC, Zheng J, Beauchamp MS, Collinger JL, Pouratian N, McGuire AL, Sheth SA, Adolphs R, Andersen RA, Baltuch G, Brunner P, Cash SS, Chang E, Collinger JL, Crone N, Fedorenko E, Fried I, Gold J, Henderson J, Hochberg L, Howard M, Kahana MJ, Magnotti J, Mamelak A, Pouratian N, Richardson RM, Rutishauser U, Schalk G, Schroeder C, Shenoy K, Sheth SA, Suthana N, Tandon N, Williams ZM, Wolpaw J. Benefits of sharing neurophysiology data from the BRAIN Initiative Research Opportunities in Humans Consortium. Neuron 2023;111(23):3710–5. http://dx.doi.org/10.1016/j.neuron.2023.09.029, URL https://linkinghub.elsevier.com/retrieve/pii/S0896627323007171.

[22] Johnson BC, Gambini S, Izyumin I, Moin A, Zhou A, Alexandrov G, Santacruz SR, Rabaey JM, Carmena JM, Muller R. An implantable 700μ w 64-channel neuromodulation IC for simultaneous recording and stimulation with rapid artifact recovery. In: 2017 symposium on VLSI circuits. 2017, p. C48–9. http://dx.doi.org/10.23919/VLSIC.2017.8008543, URL https://ieeexplore.ieee.org/document/8008543.

[23] Zhou A, Santacruz SR, Johnson BC, Alexandrov G, Moin A, Burghardt FL, Rabaey JM, Carmena JM, Muller R. A wireless and artefact-free 128-channel neuromodulation device for closed-loop stimulation and recording in non-human primates. Nat Biomed Eng 2019;3(1):15–26. http://dx.doi.org/10.1038/s41551-018-0323-x, URL https://www.nature.com/articles/s41551-018-0323-x.

[24] Jiang D, Cirmirakis D, Schormans M, Perkins TA, Donaldson N, Demosthenous A. An integrated passive phase-shift keying modulator for biomedical implants with power telemetry over a single inductive link. IEEE Trans Biomed Circuits Syst 2017;11(1):64–77. http://dx.doi.org/10.1109/TBCAS.2016.2580513.

[25] Zhou L, Donaldson N. A fast passive data transmission method for eng telemetry. Neuromodulation 2003;6(2):116–21. http://dx.doi.org/10.1046/j.1525-1403.2003.03018.x.

[26] for surgery active implantable medical devices part 1 Implants. General requirements for safety, marking and for information to be provided by the manufacturer, international standard. 2014.

[27] Limited Cochlear. Nucleus® 7 sound processor user guide (CP1000). Sydney, Australia, Cochlear Limited; 2017, URL https://www.cochlear.com.

[28] Ella A, Keller M. Construction of an MRI 3D high resolution sheep brain template. Magn Reson Imaging 2015;33(10):1329–37. http://dx.doi.org/10.1016/j.mri.2015.09.001.

[29] Ella A, Delgadillo JA, Chemineau P, Keller M. Computation of a high-resolution MRI 3D stereotaxic atlas of the sheep brain. J Comp Neurol 2017;525(3):676–92. http://dx.doi.org/10.1002/cne.24079.

[30] Rudoler JH, Herweg NA, Kahana MJ. Hippocampal theta and Episodic Memory. J Neurosci 2023;43(4):613–20. http://dx.doi.org/10.1523/JNEUROSCI.1045-22.2022, URL https://www.jneurosci.org/lookup/doi/10.1523/JNEUROSCI.1045-22.2022.

[31] Raicevich G, Burwood E, Dillon H. Taking the pressure off bone conduction hearing aid users. Aust New Zealand J Audiol 2008;30(2):113–8, published 2008. URL https://researchers.mq.edu.au/en/publications/taking-the-pressure-off-bone-conduction-hearing-aid-users.

[32] Haufe S, Meinecke F, Görgen K, Dähne S, Haynes J-D, Blankertz B, Bießmann F. On the interpretation of weight vectors of linear models in multivariate neuroimaging. NeuroImage 2014;87:96–110. http://dx.doi.org/10.1016/j.neuroimage.2013.10.067, URL https://linkinghub.elsevier.com/retrieve/pii/S1053811913010914.

[33] Long NM, Kahana MJ. Modulation of task demands suggests that semantic processing interferes with the formation of episodic associations. J Exp Psychol [Learn Mem Cogn] 2017;43(2):167–76. http://dx.doi.org/10.1037/xlm0000300.

[34] Mohan UR, Watrous AJ, Miller JF, Lega BC, Sperling MR, Worrell GA, Gross RE, Zaghloul KA, Jobst BC, Davis KA, Sheth SA, Stein JM, Das SR, Gorniak R, Wanda PA, Rizzuto DS, Kahana MJ, Jacobs J. The effects of direct brain stimulation in humans depend on frequency, amplitude, and white-matter proximity. Brain Stimul 2020;13(5):1183–95. http://dx.doi.org/10.1016/j.brs.2020.05.009, number: 5 MohaEtal20. URL https://linkinghub.elsevier.com/retrieve/pii/S1935861X2030108X.

[35] Manning JR, Jacobs J, Fried I, Kahana MJ. Broadband shifts in local field potential power spectra are correlated with single-neuron spiking in humans. J Neurosci 2009;29(43):13613–20. http://dx.doi.org/10.1523/JNEUROSCI.2041-09.2009.

[36] Benjamini Y, Yekutieli D. The control of the false discovery rate in multiple testing under dependency. In: Annals of statistics. 2001, p. 1165–88, Publisher: JSTOR.

[37] Nair DR, Laxer KD, Weber PB, Murro AM, Park YD, Barkley GL, Smith BJ, Gwinn RP, Doherty MJ, Noe KH, Zimmerman RS, Bergey GK, Anderson WS, Heck C, Liu CY, Lee RW, Sadler T, Duckrow RB, Hirsch L, Wharen RE, Tatum W, Srinivasan S, McKhann GM, Agostini MA, Alexopoulos AV, Jobst BC, Roberts DW, Salanova V, Witt TC, Cash SS, Cole AJ, Worrell GA, Lundstrom BN, Edwards JC, Halford JJ, Spencer DC, Ernst L, Skidmore CT, Sperling MR, Miller I, Geller EB, Berg MJ, Fessler AJ, Rutecki P, Goldman AM, Mizrahi EM, Gross RE, Shields DC, Schwartz TH, Labar DR, Fountain NB, Elias WJ, Olejniczak PW, Villemarette-Pittman NR, Eisenschenk S, Roper SN, Boggs JG, Courtney TA, Sun F-T, Seale CG, Miller KL, Skarpaas TL, Morrell MJ, Nair DR. Nine-year prospective efficacy

and safety of brain-responsive neurostimulation for focal epilepsy. Neurology 2020;95(9):e1244–56. http://dx.doi.org/10.1212/WNL.0000000000010154.

[38] Roa JA, Marcuse L, Fields M, Vega-Talbott ML, Yoo JY, Wolf SM, McGoldrick P, Ghatan S, Panov F. Long-term outcomes after responsive neurostimulation for treatment of refractory epilepsy: a single-center experience of 100 cases.. J Neurosurg 2023;139(5):1463–70. http://dx.doi.org/10.3171/2023.2.JNS222116.

[39] Stull SW, Mogle J, Bertz JW, Burgess-Hull AJ, Panlilio LV, Lanza ST, Preston KL, Epstein DH. Variability in intensively assessed mood: Systematic sources and factor structure in outpatients with opioid use disorder. Psychol Assess 2022;34(10):966–77. http://dx.doi.org/10.1037/pas0001160, number: 10 StulEtal22.

[40] Sakon JJ, Halpern DJ, Schonhaut DR, Kahana MJ. Human hippocampal ripples signal encoding of episodic memories. J Neurosci 2024. http://dx.doi.org/10.1523/JNEUROSCI.0111-23.2023, e0111232023. URL https://www.jneurosci.org/lookup/doi/10.1523/JNEUROSCI.0111-23.2023.

[41] Sanger T. R. Henry ZT, Park MC, Darrow D, McGovern RA, Netoff TI. Neural signal data collection and analysis of percept™, PC BrainSense recordings for thalamic stimulation in epilepsy. J Neural Eng 2024;21(1):012001. http://dx.doi.org/10.1088/1741-2552/ad1dc3.

[42] Heck CN, King-Stephens D, Massey AD, Nair DR, Jobst BC, Barkley GL, Salanova V, Cole AJ, Smith MC, Gwinn RP, Skidmore C, VanNess PC, Bergey GK, Park YD, Miller I, Geller E, Rutecki PA, Zimmerman R, Spencer DC, Goldman A, Edwards JC, Leiphart JW, Wharen RE, Fessler J, Fountain NB, Worrell GA, Gross RE, Eisenschenk S, Duckrow RB, Hirsch LJ, Bazil C, O'Donovan CA, Sun FT, Courtney TA, Seale CG, Morrell MJ. Two-year seizure reduction in adults with medically intractable partial onset epilepsy treated with responsive neurostimulation: Final results of the rns system pivotal trial. Epilepsia 2014;55(3):432–41. http://dx.doi.org/10.1111/epi.12534.

[43] Meisenhelter S, Nair NA, Gonsalves EC, Leech KA, Nowell GS, Brunell NB, Ojemann JG, Miller BJ. Cognitive tasks and human ambulatory electrocorticography: Tracking day-to-day cognition after device implantation. J Psychiatr Res 2019;119:199–206. http://dx.doi.org/10.1016/j.jpsychires.2019.06.012.

[44] NeuroPace Inc. RNS® System Physician Manual: For the RNS® Neurostimulator Model RNS-320. Mountain View, CA, document Number: DN 1016734; Revision: 11; Revision Date: 2018-06, NeuroPace, Inc.; 2018, URL www.NeuroPace.com.

[45] Stanslaski S, Herron J, Chouinard T, Bourget D, Isaacson B, Kremen V, Opri E, Drew W, Brinkmann BH, Gunduz A, Adamski T, Worrell GA, Denison T. A chronically implantable neural coprocessor for investigating the treatment of neurological disorders. IEEE Trans Biomed Circuits Syst 2018;12(6):1230–45. http://dx.doi.org/10.1109/TBCAS.2018.2880148.

[46] Goyal A, Goetz S, Stanslaski S, Oh Y, Rusheen AE, Klassen B, Miller K, Blaha CD, Bennet KE, Lee K. The development of an implantable deep brain stimulation device with simultaneous chronic electrophysiological recording and stimulation in humans. Biosens Bioelectron 2021;176:112888. http://dx.doi.org/10.1016/j.bios.2020.112888, published in final edited form as: Biosens Bioelectron. 2021 March 15; 176: 112888.

[47] Cho H, Benjaber M, Gkogkidis CA, Buchheit M, Ruiz-Rodríguez JF, Grannan BL, Weaver KE, Ko AL, Cramer SC, Ojemann JG, Denison T, Herron JA. Development and evaluation of a real-time phase-triggered stimulation algorithm for the cortec brain interchange. IEEE Trans Neural Syst Rehabil Eng 2024;32:3625. http://dx.doi.org/10.1109/TNSRE.2024.3459801, date of publication 12 2024.

[48] CorTec Neuro. Brain interchange implantable system data sheet. 2025, https://cortec-neuro.com/brain-interchange-system/implantable-system/. [Accessed 17 October 2025].

[49] Oxley TJ, Opie NL, John SE, Rind GS, Ronayne SM, Wheeler TL, Judy JW, McDonald AJ, Dornom A, Lovell TJH, Steward C, Garrett DJ, Moffat BA, Lui EH, Yassi N, Campbell BCV, Wong YT, Fox KE, Nurse ES, Bennett IE, Liyanage KA, van der Nagel NR, Perucca P, Ahnood A, Gill KP, Yan B, Churilov L, French CR, Desmond PM, Horne MK, Kiers L, Prawer S, Davis SM, Burkitt AN, Mitchell PJ, Grayden DB, May CN, O'Brien TJ. Minimally invasive endovascular stent-electrode array for high-fidelity, chronic recordings of cortical neural activity. Nature Biotechnol 2016;34(3):320–7. http://dx.doi.org/10.1038/nbt.3428.

[50] Mitchell P, Lee SCM, Yoo PE, Morokoff A, Sharma RP, Williams DL, MacIsaac C, Howard ME, Irving L, Vrljic I, Williams C, Bush S, Balabanski AH, Drummond KJ, Desmond P, Weber D, Denison T, Mathers S, O'Brien TJ, Mocco J, Grayden DB, Liebeskind DS, Opie NL, Oxley TJ, Campbell BCV. Assessment of safety of a fully implanted endovascular brain-computer interface for severe paralysis in 4 patients: The stentrode with thought-controlled digital switch (switch) study. JAMA Neurol 2023;80(3):270–8. http://dx.doi.org/10.1001/jamaneurol.2022.4847, published online January 9 2023. Corrected on March 27 2023.

[51] Musk E, Neuralink. An integrated brain-machine interface platform with thousands of channels. J Med Internet Res 2019;21(10):e16194. http://dx.doi.org/10.2196/16194, published 31.10.19. URL http://www.jmir.org/2019/10/e16194/.

[52] Haji M, Mutyala A. Elon musk's neuralink N1: Inside the silicon. 2023, https://mikaelhaji.medium.com/a-technical-deep-dive-on-elon-musks-neuralink-in-40-mins-71e1100f54d4. [Accessed 16 October 2025].